Nanoscale

PAPER

View Article Online
View Journal | View Issue

Cite this: *Nanoscale*, 2025, **17**, 3402

Monodisperse Pt nanoparticle arrays *via* block copolymer nanopatterning and their reaction kinetics on CO oxidation†

Geon Gug Yang,[a] Hyeong Min Jin,[b] Minsu Park,[c] Minha Kim,[c] Dong-Wook Shin,[c] Sang Ouk Kim,*[a] WooChul Jung *[d] and Siwon Lee *[c]

Received 2nd September 2024,
Accepted 2nd December 2024

DOI: 10.1039/d4nr03582h

rsc.li/nanoscale

Advances in nanotechnology are able to open up new prospects for catalysis, particularly through the development of catalytic systems featuring precisely controlled size and distribution of metal nanoparticles. In this study, we prepared a model catalytic system, where monodisperse Pt nanoparticles, approximately 8 nm in size, were uniformly distributed onto CeO_2 and SiO_x/Si substrates *via* block copolymer (BCP) nanopatterning. To address the validity of these catalysts, we conducted a case study on CO oxidation in a continuous flow reactor, investigated the reaction kinetics, and compared our observations with those reported in the literature. The reaction orders for CO and O_2, activation energy, and turnover frequency values on these catalysts were in good agreement with those with well-established kinetic data, demonstrating consistency and reliability. These results suggest a potential application of the BCP-nanopatterned catalyst as a model system for fundamental studies in various catalytic processes.

Introduction

Block copolymer (BCP) self-assembly has offered a viable nanopatterning method that exhibits well-defined and periodic nanoscale features in a thin-film geometry, and this technology has been exploited for a wide range of applications, including semiconductor devices, optoelectronic devices, sensors, and catalysts.[1–5] Nanoscale control is typically achieved by the nature of BCPs, which consist of covalently linked chemically distinct polymeric blocks that spontaneously undergo microphase separation to form monodisperse, densely periodic nanostructures (5–100 nm). Appropriate control of the BCP chain length and the volume fraction of each block offers size-tunable, diverse nanostructures, including lamella, cylinders, and spheres.[6,7] In particular, using vertically aligned, hexagonally packed cylindrical structures as pattern templates allows for the easy formation of the nanoarrays of monodisperse nanoparticles (polydispersity <0.1).[8–10]

One application that can exploit the advantages from this well-defined particle size and distribution is a model system for electrocatalysis. For instance, in one literature report,[11] various metal nanoparticle (NP) catalysts (*i.e.*, Pt, Pd, Au, and Co) were uniformly introduced on solid oxide fuel cell electrodes *via* BCP nanopatterning. In that study, the authors changed only the composition and thus successfully unraveled the inherent electrocatalytic properties of the mixed-conducting oxide ($Sm_{0.2}Ce_{0.8}O_{1.9-\delta}$, samarium doped ceria, SDC). Given the heterogeneous distribution of the industrially relevant catalysts, which hinders the understanding of the relationship between the material structure and function, the utilization of the model system proved valuable in providing novel insights that would otherwise be challenging to comprehend. In some cases, alternative methods apart from BCP nanopatterning have been employed for similar purposes. For example, Larrazábal *et al.* used an electron beam evaporation to fabricate a model electrode having uniform size of copper–indium particles for the CO_2 reduction reaction.[12] The authors elucidated the underlying reaction mechanism *via* that system; however, the usage of relatively larger micrometer-scale materials may pose limitations in directly correlating the findings to real-world catalysts. Meanwhile, the BCP achieves nanometer scale patterns even below 10 nm, which is a catalytically relevant size.

In the realm of chemical catalysis, precisely defined model systems through polymer templates are also frequently utilized to investigate the reaction mechanisms underlying the process of interest. In some studies,[13–15] the uses of engineered mono-

[a]*Department of Materials Science and Engineering, Korea Advanced Institute of Science and Technology, Daejeon 34141, Republic of Korea*
[b]*Department of Organic Materials Engineering, Chungnam National University, Daejeon 34134, Republic of Korea*
[c]*Department of Materials Science and Engineering, Hanbat National University, Daejeon 34158, Republic of Korea. E-mail: swlee@hanbat.ac.kr*
[d]*Department of Materials Science and Engineering, Seoul National University, Seoul 08826, Republic of Korea. E-mail: wcjung@snu.ac.kr*
† Electronic supplementary information (ESI) available. See DOI: https://doi.org/10.1039/d4nr03582h

disperse metal nanoparticles (such as Pt, Pd, and Ni) were employed to quantify the interface between metals and oxides (*e.g.*, CeO_2 and Al_2O_3) as well as the metal surface. In those studies, the authors analyzed the correlation between the quantified reaction sites and reactivity, and identified key active sites for reactions including CO oxidation, CH_4 oxidation, dry reforming of methane (DRM), and water–gas shift (WGS). Other studies used bimetal catalysts with controlled sizes[16] or even metal catalysts with tailored shapes,[17] which were proved by investigations to be the reaction paths governing CO oxidation on the catalysts.

However, in numerous cases, including those in the aforementioned studies, capping agents (such as ionic, amine, and/or polymeric surfactants) are typically employed for synthesizing well-defined metal catalysts,[18,19] and the utilization of these surfactants results in the poisoning of the catalyst surface.[20] To overcome these issues, an alternative adopted approach involving the growth of metal nanoparticles on an aligned uniform pore scaffold through conventional methods like incipient wetness impregnation[19,21,22] or the synthesis of a metal@oxide core–shell structure was used.[23–25] While these approaches may be free of ligands through thermal treatment, their complicated structures often restrict the interpretation of the observed outcomes, demanding the utilization of state-of-the-art analytical techniques.[15] Given the fact that capping agents are unnecessary in the BCP nanopatterning (as metal ions directly bind into a specific spot through electrostatic attraction) and the structure of the material system is straightforward, the BCP nanopatterning technique offers benefits in fabricating model structures for numerous catalytic processes.

Yet, there remain limited cases using BCP nanopatterning for catalytic research. Moreover, even in the existing case, the experiments were conducted in a batch reactor[26] in which the reaction kinetics may vary due to changes of the state of the system over time.[27] Thus, the relevance of the BCP nanopatterned catalyst for modeling the behavior of a conventional high-surface-area supported catalyst, to the best of our knowledge, has yet to be demonstrated. In this study, we synthesized Pt/CeO_2 and Pt/SiO_x by an inch-scale large-area process using BCP nanopatterning, and examined the catalysts in a continuous flow reactor to analyze reaction kinetics over CO oxidation. CO oxidation is chosen as a case study due to its well-established kinetics for both Pt/CeO_2 and Pt/inert supports. Our approach allows direct comparison of reaction kinetics, including reaction order, activation energy, and turnover frequency (TOF), measured on BCP-nanopatterned catalysts with those observed on more realistic supported metal catalysts. This provides convincing evidence that the BCP-nanopatterned catalyst is applicable for a model catalytic system.

Experimental

The two substrates for Pt NP arrays were composed of 2-inch single-crystal Si wafer with a deposited CeO_2 and native SiO_x film on it. The CeO_2 film was introduced by pulsed laser deposition (PLD) utilizing a KrF 248 nm excimer laser (Coherent COMPex Pro 205). The PLD process was operated at a pulse frequency of 10 Hz and a pulse energy of 250 mJ per pulse. Initially, the PLD chamber was heated to 823 K with a ramping rate of 8 K per minute, and the oxygen partial pressure in the chamber was set to be 10 mTorr. The deposition of CeO_2 was then performed for a specified duration (35 minutes) to achieve a targeted thickness of approximately 600 nm. For SiO_x, the native oxide formed on the Si wafer was utilized without any additional treatment.

Pt NP arrays were subsequently introduced onto each substrate by using a BCP self-assembly technique. Polystyrene-*block*-poly(4-vinylpyridine) (PS-*b*-P4VP, M_n: 25 kg mol^{-1}-*b*-10 kg mol^{-1}, purchased from Polymer Source Inc.) BCP was dissolved in a toluene and tetrahydrofuran (THF) mixed solvent with a 3 : 1 weight ratio, at 0.5 wt%. The PS-*b*-P4VP thin film was spin coated onto a CeO_2 and Si-wafer substrate. The BCP thin film was solvent vapor annealed in a toluene and THF mixture (1 : 4 volume ratio) to induce vertically aligned hexagonal cylinder P4VP arrays.[8] The prepared substrate was then immersed in a 1 mM Pt precursor solution, where K_2PtCl_4 was dissolved in a 1 vol% HCl solution, to selectively load $PtCl_4^{2-}$ ions into the protonated P4VP block. After loading the Pt precursor, the BCP film was etched using O_2 reactive ion etching (50 sccm O_2 and 50 W radio frequency power) for 1 minute. The nanostructure of each sample was analyzed using scanning electron microscopy (SEM) with SU-8230 and S-4800 instruments manufactured by Hitachi and transmission electron microscopy (TEM, HF5000, Hitachi). To evaluate the particle size distribution, ImageJ software was utilized to estimate the projected area of each Pt particle by analyzing the brightness and contrast difference between Pt and the substrate. Assuming a circular shape for each particle, the average diameter and standard deviation were calculated based on the measured area from over 150 particles. To determine particle density, we manually counted the number of particles in the SEM images and measured the area, in which the particle existed, using a scale bar.

The catalytic performance in CO oxidation was assessed in a quartz microreactor having an outer diameter (OD) of 1/2 inches. For each catalytic evaluation, three wafers (each with a diameter of 2 inches) were used, cleaved into small pieces, and positioned between quartz wool plugs. Control over the reactant mixture composition was achieved by adjusting the flow rates of CO, O_2, and Ar using mass flow controllers (MFC), while maintaining a constant total flow rate of 50, 75, or 100 mL min^{-1}. Real-time monitoring of both reactants and products was conducted using a quadrupole mass spectrometer (PFEIFFER Vacuum GSD320) connected to the microreactor outlet. The light-off curves were generated by incrementally raising the reaction temperature from ambient to 573 K at a ramping rate of 3 K min^{-1} while introducing reactant gases. The CO conversion ratio (%) was defined as $100 \times (mol_{CO,in} - mol_{CO,out})/mol_{CO,in}$. Turnover frequencies (TOFs) were determined by normalizing the number of produced CO_2 molecules per second to the number of Pt atoms (either at the surface or

within the volume). The TOF formula is defined as $\mathrm{TOF} = \frac{n_{\mathrm{product}}(\text{number of product molecules})}{n_{\mathrm{Pt\,atoms}}(\text{number of Pt atoms}) \times \text{time}}\,(\mathrm{s}^{-1})$. The intensity of CO was corrected by accounting for the contribution of the cracking fragment of CO_2 (11.4%) using the mass concentration determination (MCD) mode.

Results and discussion

Preparation of the Pt nanoparticle arrays

We first prepared two different carriers for Pt NPs: one comprised a Si-wafer with a native silicon oxide layer, while the other featured a Si-wafer with a CeO_2 film atop. The CeO_2 film was deposited *via* PLD, with a thickness measuring approximately 600 nm (Fig. S1†). Pt NP arrays were then introduced onto the two prepared carriers, and Fig. 1 shows a schematic illustration of this process. For the fabrication of the uniformly aligned Pt NPs, we employed PS-*b*-P4VP BCP. This consideration was made due to its small domain size (cylinder center to center distance: ~36 nm) resulting from a high Flory–Huggins parameter, as well as the ion adsorption properties of the protonated P4VP block. The vertical alignment of the P4VP cylindrical morphology was induced by solvent vapor annealing using a judicious mixture of THF and toluene solvent (see step 1 in Fig. 1). Considering the fact that the morphology of BCP phase separation is highly dependent on the thickness profile of the BCP film,[28,29] the surface roughness of the underlying substrate should be minimized to induce uniform phase separation across the substrate. Top-view image of the resultant BCP film showed a vertically well-aligned cylindrical nanodomain (Fig. S2†), indicating that the CeO_2 layer was uniformly deposited on the Si-wafer with low surface roughness. P4VP was then immersed in an acidic solution and protonated *via* lone pair electrons on the pyridinic nitrogen. This protonation of pyridinic nitrogen results in a partial positive charge, facilitating the selective adsorption of the negatively charged metal precursor onto the P4VP block (see step 2 in Fig. 1). As a final step, we used oxygen plasma treatment on the Pt-adsorbed BCP film to eliminate the BCP template and leave only the Pt NP arrays. Since the Pt precursor ($PtCl_4^{2-}$ ions) was only adsorbed on the P4VP domain, the uniform Pt particle size and distribution in the array were ensured along the P4VP block provided by the spontaneous phase separation behavior (see step 3 in Fig. 1).

Fig. 2a–d show SEM images of the samples prepared in this study, which were Pt/CeO_2 (Fig. 2a and b) and Pt/SiO_x (Fig. 2c and d), respectively. In both cases, Pt NPs were evenly synthesized across the entire substrate surface, exhibiting uniform particle size and distribution (8.0 ± 1.0 nm for Pt/CeO_2 and 7.8 ± 0.4 nm for Pt/SiO_x), similar to the Pt arrays previously reported with compositional evidence obtained *via* top-down TEM observations.[9] The particle density (with a unit of $\#/m^2$) was estimated to be 1×10^{15} for both Pt/CeO_2 and Pt/SiO_x. Given the capability of the well-defined NP arrays to offer a quantitative analysis of metal particle surfaces and metal–oxide interfaces, which are commonly regarded as key active sites in various catalytic processes, it becomes imperative to confirm the stability of the array structure prior to the catalytic test. In this regard, since we constrained the maximum reaction temperature to 573 K, all samples were subjected to heat treatment at 573 K for 2 hours, and as demonstrated in Fig. 2, this ensured that the size and distribution of Pt nanoarrays were well preserved. Note that due to the low specific surface area of the two-dimensional sample, the conventional method for measuring metal dispersion, such as CO and H_2 chemisorption, were limited in this study. For a more detailed structural analysis of the nanoparticle, we carried out TEM and scanning transmission electron microscopy (STEM) analyses along with energy dispersive X-ray spectroscopy (EDS) mapping. Fig. 2e and f show high-resolution TEM (HR-TEM) images exhibiting the lattice fringes of Pt/CeO_2 and Pt/SiO_x, respectively, along with their corresponding Fast Fourier Transform (FFT) patterns. In Fig. 2e, the FFT pattern from the

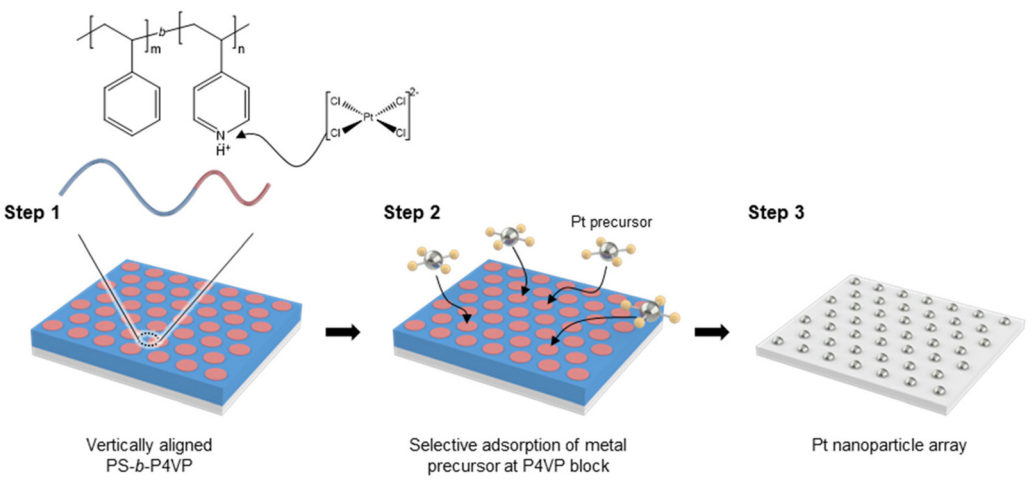

Fig. 1 Schematic flowchart of the synthetic procedures of Pt nanoparticle arrays *via* the block copolymer nanopatterning technique.

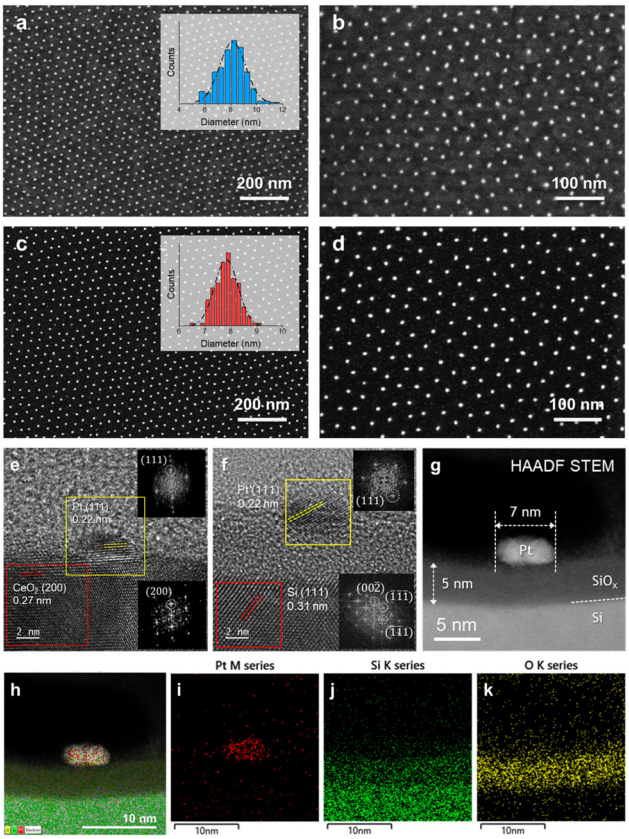

Fig. 2 SEM images of the Pt NP arrays from BCP self-assembly on (a and b) CeO_2 and (c and d) SiO_x. (e) HR-TEM image of Pt/CeO_2. (f) HR-TEM and (g) HAADF-STEM images of Pt/SiO_x with (h–k) EDS map data.

region within the yellow-colored square corresponding to Pt reveals a lattice spacing of 0.22 nm, which matches the lattice spacing of the Pt (111) plane. The FFT pattern from the crystalline region beneath the Pt (highlighted in a red square) indicated a lattice spacing of 0.27 nm, corresponding to the CeO_2 (200) plane. Similarly, in Fig. 2f, for Pt/SiO_x, the FFT patterns for Pt and the single-crystal Si wafer show the associated lattice spacings (*i.e.*, 0.22 nm for Pt (111) and 0.31 nm for Si (111)). The native oxide layer between Pt and the Si wafer was confirmed to be amorphous (Fig. S3†), with an approximate thickness of 5 nm. Fig. 2g–k show a high-angle annular dark-field scanning transmission electron microscopy (HAADF-STEM) image and EDS map data for Pt/SiO_x, demonstrating the distribution of each element and verifying that the native oxide layer beneath the Pt was indeed SiO_x. Similarly, Pt/CeO_2 was analyzed using STEM and EDS mapping, revealing the spatial distribution of individual elements (Fig. S4†).

Kinetics analysis of the Pt/SiO_x sample

The catalytic properties of Pt NP arrays were evaluated for the CO oxidation reaction across a temperature range from ambient conditions (298 K) up to 573 K. This study utilized CO oxidation as a case study because CO oxidation has well-established reaction kinetics for Pt, facilitating straightforward comparisons with the literature, and has an industrial significance of this reaction, particularly in applications like exhaust gas purification catalysts.

Initially, Pt NP arrays supported on SiO_x without a CeO_2 promoter were examined to determine if the catalysts exhibit similar performance characteristics in the CO oxidation reaction compared to those reported in the literature (*e.g.*, Pt/γ-Al_2O_3 and Pt/SiO_2). Before initiating the reaction, the sample was preheated under an oxygen atmosphere at 573 K for 30 minutes. Fig. 3a illustrates the light-off curves of the CO oxidation over Pt/SiO_x. The feed gas comprised a mixture containing 7.6 Torr of CO and 60.8 Torr of O_2, with the balance being Ar. As shown in the figure, we first examined the effect of flow

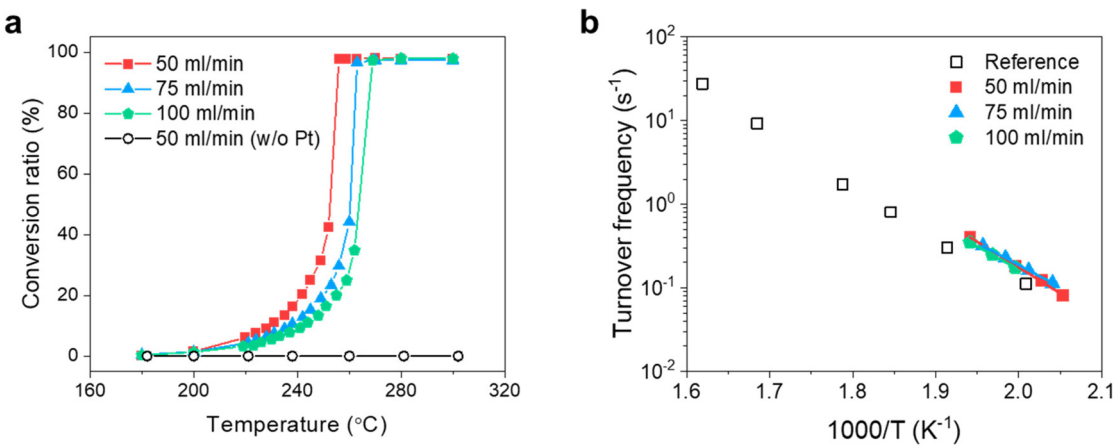

Fig. 3 (a) The light-off curves for CO oxidation on Pt NP arrays under various flow rates ranging from 50 ml min^{-1} to 100 ml min^{-1}, with a gas mixture of 7.6 Torr of CO, 60.8 Torr of O_2, and Ar. The unfilled black circles represent the results observed on a Si wafer without Pt NP arrays. (b) The specific reaction rates as a function of the inverse temperature for Pt NP arrays, alongside reference data measured on Pt(100)[30] (denoted by empty black squares). Adapted with permission from *J. Phys. Chem.* 1988, **92**, 5213–5221. Copyright 1988 American Chemical Society. Note that the measured specific rates were adjusted to compare with the reference data, considering the fact that rates on unpromoted Pt have been reported to exhibit linear dependencies on $p[O_2]$ and $p[CO]$.

rate variation on the reaction by adjusting the total flow rate from 50 to 100 mL min^{-1} for the Pt/SiO_x sample. The observation revealed that the reaction commenced around 473 K, with complete conversion of CO to CO_2 occurring before 543 K, regardless of the flow rate. As the flow rate increased, the light-off curve shifted toward the higher temperature region. It is reasonable behavior given the fact that the total quantity of CO available for reaction increases proportionally with the flow rate. Note that the reference Si wafer without Pt was denoted by black unfiled circle symbols, revealing no notable reaction activity up to 573 K. This clearly indicates that all observed reactions occurred on the Pt NP arrays.

Fig. 3b shows TOF values (measured as the number of CO_2 formed/the number of Pt atoms on the surface/second *versus* 1000/T(K)) acquired from a series of Pt/Si catalyst samples, where the total flow rate was varied between 50 and 100 mL min^{-1}. Data from Pt single crystal experiments (denoted by unfilled square symbols)[30,31] are included for comparative analysis. Note that the literature data were collected under a CO/O_2 ratio of 2, which represents the stoichiometric ratio for CO oxidation. In contrast, the results shown in Fig. 3a were obtained with a CO/O_2 ratio of 1/8. Thus, considering the positive first-order dependency of oxygen partial pressure in CO oxidation on Pt, adjustments were made to the TOF to ensure accurate comparison (Fig. 3b). For the Pt atom numbers on the surface for TOF calculation, since dispersion analysis using chemisorption is somewhat limited for two-dimensional materials, in this study, the geometric shape of the Pt NPs was assumed to be a hemisphere, and the number of Pt atoms on the surface was determined using the cross-sectional area of atomic platinum. This assumption stems from the benefits of the BCP process, wherein the Pt NPs exhibit uniform distribution per unit area, and the size difference between particles is minimal and almost constant. The hemispherical geometry of the BCP nanoparticles was also previously confirmed in the literature.[9,11,32] The result data revealed good agreement in TOF values between the Pt NPs examined in this study and Pt single crystal observed elsewhere.[30,31] Therefore, Pt NP arrays closely matched well with the reference and exhibited no flow rate effect under the reaction conditions studied, indicating that the amount of CO_2 produced per unit time on Pt was the same. This clearly demonstrates that the reaction occurred predominantly on the Pt surface, and that all Pt NPs participated in the reaction without mass transfer limitation. The apparent activation energy ($E_{app.}$) for Pt/SiO_x, calculated from the Arrhenius plot $k = A^* e^{\left(-\frac{E_{app}}{RT}\right)}$, was determined to be 108.5 kJ mol^{-1} (equivalent to 25.9 in kcal mol^{-1}). Here, k represents the reaction rate constant, A is the pre-exponential factor, R is the gas constant, and T denotes the temperature. As will be discussed later, this value is also similar to the one reported in the literature (see Table 1). Overall, the Pt NP system based on the BCP technique effectively represents a conventional Pt catalyst.

Under some conditions, the Pt catalyst demonstrates sensitivity to both CO and O_2 partial pressures in the CO oxidation.

Table 1 Kinetic data of the sample along with the values reported elsewhere

Catalysts	E_a (kJ mol^{-1})	E_a (kcal mol^{-1})	Reaction order	
			In CO	In O_2
This work (Pt/SiO_x)	108.5	25.9	−0.48 to −0.96	0.99
Pt (diluted with quartz)[37]	99.4		−0.8	1.01
Pt/SiO_2 [38]	133		−1.0	1.0
Pt/SiO_2 [39]	110 ± 10			
Pt/SiO_2 [40]		23.2		
Pt/SiO_2 [41]		26.0		
Pt(100)[30]			0 to −0.9	1.0 ± 0.1
Pt wire[42]			−1.0	1.0

For example, regarding CO, it shows a negative first-order dependency, where reactivity diminishes with increasing partial pressure of CO due to the poisoning of the Pt surface, whereas, with oxygen, it exhibits a positive first-order dependency. Therefore, taking these characteristics, to further comprehend our Pt catalyst, we investigated the dependency of CO and O_2 on Pt NP arrays. Fig. 4a shows the light-off curves of the CO oxidation over Pt/SiO_x, and the results were obtained by varying the partial pressure of oxygen from 7.6 to 38 Torr, while maintaining the partial pressure of CO at 0.76 Torr. The overall flow rate was kept constant at 100 mL min^{-1} using Ar as a balance gas. Notably, regardless of the partial pressure, complete conversion of CO to CO_2 occurred within 513 K. Particularly noteworthy was the observation that as the oxygen partial pressure in the feed increased, the light-off curve shifted to lower temperature ranges. This clearly indicates the promotion of the reaction by oxygen, suggesting an anticipated positive reaction order for oxygen on this catalyst.

Fig. 4b shows the TOFs, and this value was calculated by estimating the number of atoms on the Pt surface according to the aforementioned approach. This result distinctly exhibits the dependency on oxygen, and when comparing the TOF values for 7.6 and 38 Torr of oxygen at 466 K, the difference was found to be approximately 5 times. Given the fivefold increase in oxygen quantity in the feed gas, we can speculate a linear dependency. In Fig. 4c, the dependency on oxygen partial pressure (pO_2) is presented through the TOF value for the pO_2 function, where the slope indicating the reaction order was determined to be 0.99 ± 0.03, exhibiting an almost positive first order. The apparent activation energy observed was found to be on average 114.1 kJ mol^{-1} (27.2 in kcal mol^{-1}) regardless of oxygen quantity, suggesting that the reaction conditions used here did not change the apparent reaction mechanism on Pt.

Next, Fig. 4d illustrates the result of light-off curves, observing the dependence on CO partial pressure (pCO). This was achieved by varying the partial pressure of CO from 0.76 to 7.6 Torr, while maintaining the partial pressure of oxygen at 38 Torr. In contrast to the observation regarding the pO_2 dependency, the decrease in pCO shifted the light-off curves to lower

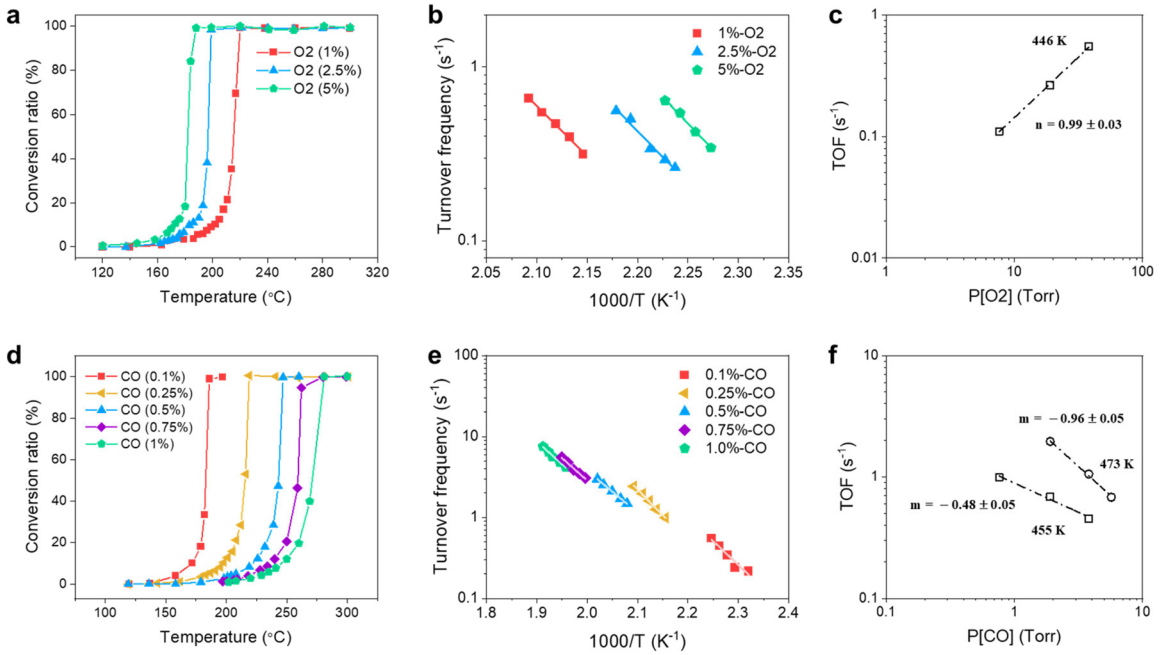

Fig. 4 (a) The light-off curves for CO oxidation on Pt NP arrays under different O_2 partial pressures ranging from 7.6 Torr (1%) to 38 Torr (5%), while keeping the CO partial pressure constant at 0.76 Torr (0.1%). The total flow rate was adjusted to 100 ml min^{-1}. (b) The specific reaction rates as a function of the inverse temperature for Pt NP arrays. (c) O_2 partial pressure dependency at 446 K. The reaction order in O_2 is 0.99 ± 0.03. (d) The light-off curves for CO oxidation on Pt NP arrays under different CO partial pressures ranging from 0.76 Torr (0.1%) to 7.6 Torr (1%), while maintaining a constant O_2 partial pressure of 38 Torr (5%). (e) The specific reaction rates as a function of the inverse temperature for Pt NP arrays. (f) CO partial pressure dependencies at 455 K and 473 K. The reaction orders in CO are −0.48 ± 0.05 at 455 K and −0.96 ± 0.05 at 473 K.

temperature ranges. Yet, since the light-off curve represents the conversion ratio of CO and the amount of CO feed varies for each measurement, relying solely on the light-off curve poses limitations in determining the *p*CO dependency. For a more detailed examination of the *p*CO dependency, the quantity of CO converted per unit time is presented in Fig. 4e. The data showed that a decrease in CO content generally corresponded to an increase in TOF value. This observation aligns with conventional knowledge and implies a negative reaction order, attributed to the strong CO adsorption onto the Pt surface, thereby poisoning it. The reaction order at 473 K depicted in Fig. 4f did indeed reveal a negative first order (−0.96 ± 0.05) in the TOF plot as a function of *p*CO. At a lower temperature of 455 K, the observed reaction order displayed a relatively weak dependency of −0.48 ± 0.05, yet still indicated a negative order. In general, Pt typically demonstrates a negative first order with respect to CO, indicating a well-established primary reaction mechanism known as the Langmuir–Hinshelwood reaction, involving the interaction between adsorbed CO and O atoms. However, previous studies have also reported a relatively weak *p*CO dependence, particularly with variations in temperature.[30,33–36] For instance, Berlowitz *et al.* reported a change in reaction order from 0.0 to −0.6 between temperatures of 425 and 490 K. The authors proposed that at lower temperatures, the surface is largely covered by CO, potentially leading to reactions occurring, at least in part, between molecular oxygen and adsorbed CO layer, resulting in a weak negative dependency on CO. All observed data demonstrated consistency and reliability, and our findings are compiled and summarized in Table 1 for comparison with previously reported observations.

Kinetics analysis of the Pt/CeO_2 sample

The Pt/CeO_2 catalyst has also been studied extensively for the CO oxidation reaction, particularly due to its capability to promote the reaction at the newly developed Pt–CeO_2 interface site. This is mostly attributed to the ability of CeO_2 to release oxygen, which becomes especially crucial when the Pt surface is hindered from reacting due to CO poisoning. In this regard, it is important to ascertain whether the interfacial reaction characteristics are well observed in the material system that we developed. If so, it will open the opportunity to utilize industrially vital catalyst materials containing CeO_2 in the form of a well-defined model system, which will facilitate a more profound understanding in future endeavors.

For this purpose, to verify if the material system prepared in this study adheres to conventional Pt/CeO_2, we first examined its *p*CO dependency by varying the partial pressure of CO while maintaining a constant partial pressure of O_2. Fig. 5a shows the Arrhenius plot results, depicting the variation in the TOF with respect to CO partial pressure for the Pt/CeO_2 sample. The overall trend showed a decline in the TOF value as the partial pressure of CO increased. However, intriguingly, when the partial pressure of CO surpassed 45.6 Torr, the TOF

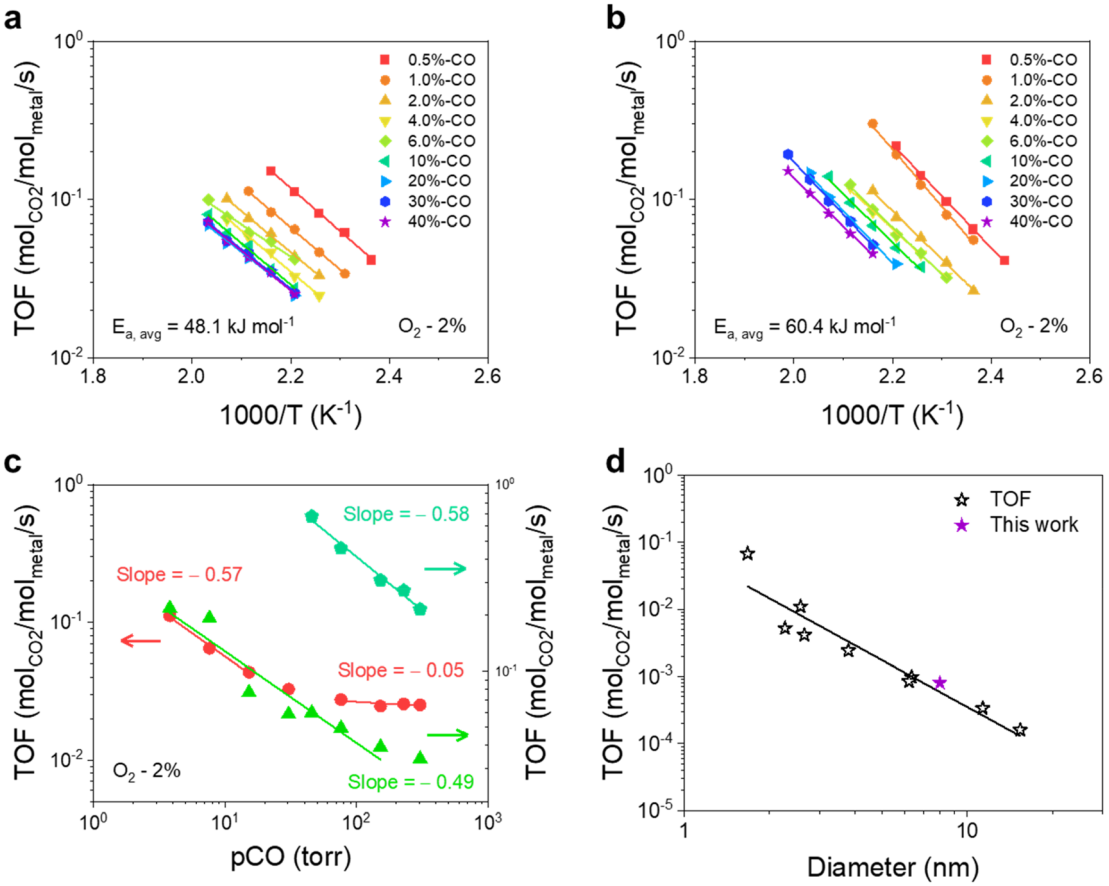

Fig. 5 The specific reaction rates as a function of the inverse temperature for Pt NP arrays supported on (a) CeO_2 and (b) SiO_x under different CO partial pressures ranging from 3.8 Torr (0.5%) to 304 Torr (40%), while keeping the O_2 partial pressure constant at 15.2 Torr (2%). The total flow rate was adjusted to 50 ml min^{-1}. (c) CO partial pressure dependencies on Pt NP arrays on CeO_2 (red circle symbols) and SiO_x (green triangle symbols) at 453 K. The green pentagon symbols represent the *p*[CO] dependency over Pt NP arrays on SiO_x at 513 K. (d) The turnover frequency (TOF) value for Pt NP arrays on CeO_2 at 353 K (purple-colored star symbol), along with reference data reported elsewhere (unfilled black star symbols).[14] Reproduced from *Science* 2013, **341**, 771–773. Reprinted with permission from AAAS. The TOF value was extrapolated using the Arrhenius plot in (a) obtained under conditions of 30.4 Torr (4%) of CO and 15.2 Torr (2%) of O_2, corresponding to a stoichiometric ratio of $CO/O_2 = 2$.

no longer decreased and remained almost the same. This observation suggests that Pt/CeO_2 would exhibit zeroth-order, under some conditions, with respect to CO partial pressure, and thus the role of the interfacial site becomes important. Fig. 5b illustrates the results of conducting the same experiment on Pt/SiO_x without CeO_2. Likewise, the overall trend demonstrates a decline in the TOF value with an increase in CO partial pressure. However, notably in this instance, the TOF continued to decrease even when the CO concentration exceeded 45.6 Torr. This suggests that CO poisoning hinders the supply of oxygen to the Pt surface, thereby making the reaction more challenging.

To better delineate the difference between the two materials, Fig. 5c shows a plot of the TOFs as a function of CO partial pressure. The change in the TOF for the Pt/Si sample, observed at 453 K, is denoted by green triangle symbols, where it showed a negative reaction order across all the observed CO partial pressures. In contrast, the TOF value for the Pt/CeO_2 sample, represented by red circle symbols, exhibited different reaction orders depending on the *p*CO range. While showing a negative order akin to Pt/SiO_x at low CO partial pressures, it gradually shifted towards a zeroth order with increasing *p*CO. This observation is consistent with what was previously expected from the Arrhenius-type plot (Fig. 5a). This variation in reaction order has been documented in previous literature,[43,44] and is known to be due to the "second mechanism" of ceria-mediated reaction. In this process, CO originates from the metal while oxygen is sourced from CeO_2, indicating the critical role of the interface between these components. Note that the extent of the interaction at this interface could vary, even with the same material, due to the structure sensitivity of CeO_2.

Given that the catalyst prepared through the BCP process exhibits uniform particle size, the investigation of the particle size dependency of the TOF for the CO oxidation would serve as further validation of this catalyst. In the literature, it has been established that the CO oxidation reaction on metals (*e.g.*, Pt, Pd, and Ni)/CeO_2 primarily take places at the metal–

ceria interface, and thus the variation in reactivity in relation to particle size has been demonstrated to be directly proportional to the extent to the interface length.[14] Fig. 5d shows the reported TOFs (black star symbols) on metal/ceria as a function of the metal particle size. In addition to this, the TOF measured in this study (a purple star symbol) under feed injection with a stoichiometric ratio (*i.e.*, $CO/O_2 = 2$) was plotted together at an average size of approximately 8 nm. As shown in the figure, it was verified that the TOF on the Pt/CeO_2 sample aligned closely with trends reported in the literature. This indicates again the role of interfacial sites in CO oxidation for Pt/CeO_2. Taking all the observations together, we found that this catalytic system mimics the behavior of a conventional Pt/CeO_2 well.

In the future, it would be anticipated that this uniformly aligned model catalytic system will lead to further insights into various commercially significant catalytic processes, including CO oxidation. Additionally, when combined with other advantages of the BCP patterning, such as control over composition,[11,32,45] particle size,[8,46,47] and density,[11] we believe that this approach would be poised to become even more valuable.

Conclusion

BCP nanopatterning facilitated the creation of uniformly aligned arrays of Pt on SiO_x and CeO_2. Both Pt/SiO_x and Pt/CeO_2 exhibited comparable reaction kinetics, which agrees with the previously reported characteristics including reaction orders, activation energy, and turnover frequency values for CO oxidation. The kinetic observations showed that the Pt surface is the dominant active area in the Pt/SiO_x sample, while the CeO_2–Pt interface importantly contributed to the reaction on Pt/CeO_2, exhibiting a secondary mechanism under some conditions. In demonstrating the consistency and reliability of the BCP nanopatterned system as a catalyst, we believe that this model structure will find applications across a range of catalytic processes, enhancing our comprehension of the underlying reaction mechanisms.

Author contributions

G. G. Yang: investigation, data curation, validation, writing – original draft, and writing – review & editing; H. M. Jin: writing – original draft and resources; M. Park: investigation; M. Kim: investigation; D.-W. Shin: investigation; S. O. Kim: conceptualization, resources, writing – original draft, writing – review & editing, funding acquisition, and supervision; W. Jung: conceptualization, resources, writing – original draft, writing – review & editing, funding acquisition, and supervision; S. Lee: conceptualization, investigation, writing – original draft, writing – review & editing, funding acquisition, and supervision.

Data availability

The authors confirm that the data supporting the findings of this study are available within the article and the ESI.†

Conflicts of interest

There are no conflicts to declare.

Acknowledgements

This work was supported by the research fund of Hanbat National University in 2023, the Korea Institute of Energy Technology Evaluation and Planning (KETEP) and the Ministry of Trade, Industry & Energy (MOTIE) of the Republic of Korea (no. RS-2024-00394769), and the National Research Foundation (NRF) of Korea grant funded by the Ministry of Science and ICT (MSIT) (RS-2023-00252444).

References

1 G. G. Yang, H. J. Choi, S. Li, J. H. Kim, K. Kwon, H. M. Jin, B. H. Kim and S. O. Kim, *Nat. Rev. Electr. Eng.*, 2024, **1**, 124–138.
2 C. Cummins, T. Ghoshal, J. D. Holmes and M. A. Morris, *Adv. Mater.*, 2016, **28**, 5586–5618.
3 G. G. Yang, H. J. Choi, K. H. Han, J. H. Kim, C. W. Lee, E. I. Jung, H. M. Jin and S. O. Kim, *ACS Appl. Mater. Interfaces*, 2022, **14**, 12011–12037.
4 C. Cummins, R. Lundy, J. J. Walsh, V. Ponsinet, G. Fleury and M. A. Morris, *Nano Today*, 2020, **35**, 100936.
5 M. Stefik, S. Guldin, S. Vignolini, U. Wiesner and U. Steiner, *Chem. Soc. Rev.*, 2015, **44**, 5076–5091.
6 L. Leibler, *Macromolecules*, 1980, **13**, 1602–1617.
7 G. H. Fredrickson and E. Helfand, *J. Chem. Phys.*, 1987, **87**, 697–705.
8 D. O. Shin, D. H. Lee, H.-S. Moon, S.-J. Jeong, J. Y. Kim, J. H. Mun, H. Cho, S. Park and S. O. Kim, *Adv. Funct. Mater.*, 2011, **21**, 250–254.
9 J. H. Mun, Y. H. Chang, D. O. Shin, J. M. Yoon, D. S. Choi, K.-M. Lee, J. Y. Kim, S. K. Cha, J. Y. Lee, J.-R. Jeong, Y.-H. Kim and S. O. Kim, *Nano Lett.*, 2013, **13**, 5720–5726.
10 N. A. Lynd, A. J. Meuler and M. A. Hillmyer, *Prog. Polym. Sci.*, 2008, **33**, 875–893.
11 Y. Choi, S. K. Cha, H. Ha, S. Lee, H. K. Seo, J. Y. Lee, H. Y. Kim, S. O. Kim and W. Jung, *Nat. Nanotechnol.*, 2019, **14**, 245–251.
12 G. O. Larrazábal, T. Shinagawa, A. J. Martín and J. Pérez-Ramírez, *Nat. Commun.*, 2018, **9**, 1477.
13 L. Foppa, T. Margossian, S. M. Kim, C. Müller, C. Copéret, K. Larmier and A. Comas-Vives, *J. Am. Chem. Soc.*, 2017, **139**, 17128–17139.

14 M. Cargnello, V. V. T. Doan-Nguyen, T. R. Gordon, R. E. Diaz, E. A. Stach, R. J. Gorte, P. Fornasiero and C. B. Murray, *Science*, 2013, **341**, 771–773.
15 S. Lee, H. Ha, K. T. Bae, S. Kim, H. Choi, J. Lee, J. H. Kim, J. Seo, J. S. Choi, Y.-R. Jo, B.-J. Kim, Y. Yang, K. T. Lee, H. Y. Kim and W. Jung, *Chem*, 2022, **8**, 815–835.
16 C. H. Wu, C. Liu, D. Su, H. L. Xin, H.-T. Fang, B. Eren, S. Zhang, C. B. Murray and M. B. Salmeron, *Nat. Catal.*, 2019, **2**, 78–85.
17 Y. Chen, J. Chen, W. Qu, C. George, M. Aouine, P. Vernoux and X. Tang, *Chem. Commun.*, 2018, **54**, 10140–10143.
18 K. An and G. A. Somorjai, *ChemCatChem*, 2012, **4**, 1512–1524.
19 K. Niesz, M. M. Koebel and G. A. Somorjai, *Inorg. Chim. Acta*, 2006, **359**, 2683–2689.
20 J. N. Kuhn, C.-K. Tsung, W. Huang and G. A. Somorjai, *J. Catal.*, 2009, **265**, 209–215.
21 S. Lee, K. Shen, C.-Y. Wang, J. M. Vohs and R. J. Gorte, *Chem. Eng. J.*, 2023, **456**, 141030.
22 C.-Y. Wang, K. Shen, R. J. Gorte and J. M. Vohs, *Inorganics*, 2022, **10**(11), 215.
23 S. Kim, S. Lee and W. Jung, *ChemCatChem*, 2019, **11**, 4653–4659.
24 S. Lee, J. Seo and W. Jung, *Nanoscale*, 2016, **8**, 10219–10228.
25 M. Cargnello, J. J. D. Jaén, J. C. H. Garrido, K. Bakhmutsky, T. Montini, J. J. C. Gámez, R. J. Gorte and P. Fornasiero, *Science*, 2012, **337**, 713–717.
26 S. M. Kim, J. H. Mun, S. W. Lee, H. An, H. Y. Kim, S. O. Kim and J. Y. Park, *Chem. Commun.*, 2018, **54**, 13734–13737.
27 K. G. Denbigh, *Trans. Faraday Soc.*, 1944, **40**, 352–373.
28 A. Knoll, A. Horvat, K. S. Lyakhova, G. Krausch, G. J. A. Sevink, A. V. Zvelindovsky and R. Magerle, *Phys. Rev. Lett.*, 2002, **89**, 035501.
29 K. Brassat and J. K. N. Lindner, *Adv. Mater. Interfaces*, 2020, **7**, 1901565.
30 P. J. Berlowitz, C. H. F. Peden and D. W. Goodman, *J. Phys. Chem.*, 1988, **92**, 5213–5221.
31 J. Rodriguez and D. Wayne Goodman, *Surf. Sci. Rep.*, 1991, **14**, 1–107.
32 S. K. Cha, J. H. Mun, T. Chang, S. Y. Kim, J. Y. Kim, H. M. Jin, J. Y. Lee, J. Shin, K. H. Kim and S. O. Kim, *ACS Nano*, 2015, **9**, 5536–5543.
33 R. C. Shishu and L. S. Kowalczyk, *Platinum Met. Rev.*, 1974, **18**, 58–64.
34 S. E. Voltz, C. R. Morgan, D. Liederman and S. M. Jacob, *Ind. Eng. Chem. Prod. Res. Dev.*, 1973, **12**, 294–301.
35 D. M. Nicholas and Y. T. Shah, *Ind. Eng. Chem. Prod. Res. Dev.*, 1976, **15**, 35–40.
36 H. Heyne and F. C. Tompkins, *Proc. R. Soc. London, Ser. A*, 1966, **292**, 460–478.
37 D. Li, H. Wang, C. Shi and X. Xu, *RSC Adv.*, 2016, **6**, 35340–35347.
38 W. D. Michalak, J. M. Krier, S. Alayoglu, J.-Y. Shin, K. An, K. Komvopoulos, Z. Liu and G. A. Somorjai, *J. Catal.*, 2014, **312**, 17–25.
39 S. M. McClure, M. Lundwall, Z. Zhou, F. Yang and D. W. Goodman, *Catal. Lett.*, 2009, **133**, 298–306.
40 S. Y. Moon, B. Naik, C.-H. Jung, K. Qadir and J. Y. Park, *Catal. Today*, 2016, **265**, 245–253.
41 D. Park, S. M. Kim, S. H. Kim, J. Y. Yun and J. Y. Park, *Appl. Catal., A*, 2014, **480**, 25–33.
42 I. Langmuir, *Trans. Faraday Soc.*, 1922, **17**, 621–654.
43 T. Bunluesin, E. S. Putna and R. J. Gorte, *Catal. Lett.*, 1996, **41**, 1–5.
44 T. Bunluesin, H. Cordatos and R. J. Gorte, *J. Catal.*, 1995, **157**, 222–226.
45 D. O. Shin, J. H. Mun, G.-T. Hwang, J. M. Yoon, J. Y. Kim, J. M. Yun, Y.-B. Yang, Y. Oh, J. Y. Lee, J. Shin, K. J. Lee, S. Park, J. U. Kim and S. O. Kim, *ACS Nano*, 2013, **7**, 8899–8907.
46 D. H. Lee, W. J. Lee and S. O. Kim, *Nano Lett.*, 2009, **9**, 1427–1432.
47 D. H. Lee, D. O. Shin, W. J. Lee and S. O. Kim, *Adv. Mater.*, 2008, **20**, 2480–2485.